Microstructural analysis of Greenland ice using a cryogenic scanning electron microscope equipped with an electron backscatter diffraction detector

Wataru SHIGEYAMA[1,2]*, Naoko NAGATSUKA[2], Tomoyuki HOMMA[3], Morimasa TAKATA[3], Kumiko GOTO-AZUMA[2,1], Ilka WEIKUSAT[4,5], Martyn R. DRURY[6], Ernst-Jan N. KUIPER[6,4], Ramona V. MATEIU[7], Nobuhiko AZUMA[3], Dorthe DAHL-JENSEN[8] and Sepp KIPFSTUHL[4]

1 Department of Polar Science, The Graduate University for Advanced Studies, SOKENDAI, 10–3 Midori-cho, Tachikawa, Tokyo, 190–8518, Japan
* shigeyama.wataru@nipr.ac.jp
2 Meteorology and Glaciology Group, National Institute of Polar Research, 10–3 Midori-cho, Tachikawa, Tokyo, 190–8518, Japan
3 Nagaoka University of Technology, 1603–1 Kamitomioka-machi, Nagaoka 940–2188, Japan
4 Alfred Wegener Institute, Helmholtz Centre for Polar and Marine Research, 27568 Bremerhaven, Germany
5 Department of Geosciences, Eberhard Karls University Tübingen, 72074 Tübingen, Germany
6 Faculty of Earth Science, Utrecht University, Postbus 80021, 3508 TA Utrecht, the Netherlands
7 Department of Chemical and Biochemical Engineering, Technical University of Denmark, Kgs Lyngby 2800, Denmark
8 Centre for Ice and Climate, Niels Bohr Institute, University of Copenhagen, Juliane Maries Vej 30, 2100 Copenhagen K, Denmark

Abstract

Mass loss from ice sheets contributes to global sea level rise, and accelerated ice flow to the oceans is one of the major causes of rapid ice sheet mass loss. To understand flow dynamics of polar ice sheets, we need to understand deformation mechanisms of the polycrystalline ice in ice sheets. Laboratory experiments have shown that deformation of polycrystalline ice occurs largely by dislocation glide, which mainly depends on crystal orientation distribution. Grain size and impurities are also important factors that determine ice deformation mechanisms. Compared with ice formed during interglacial periods, ice formed during glacial periods, especially ice that forms cloudy bands, exhibits finer grain sizes and higher impurity concentrations. A previous report suggests the deformation rate of ice containing cloudy bands is higher than that of ice without cloudy bands. To examine the microstructures and deformation histories of ice in cloudy bands, we applied the electron backscatter diffraction (EBSD) technique to samples from the Greenland Ice Sheet using an environmental scanning electron microscope (ESEM) equipped with cold stages. Prior to the EBSD analysis, we optimised our ESEM/EBSD system and performed angular error assessment using artificial ice. In terms of c- and a-axis orientation distributions and grain orientation spread, we found little difference between samples taken from a cloudy band and those taken from an adjacent layer of clear ice. However, subgrain boundary density and orientation gradients were higher in the cloudy band, suggesting that there are more dislocations in the cloudy band than in the clear ice layer.

Key words: cryogenic ESEM/EBSD, microstructure, cloudy band, Greenland Ice Sheet, NEEM ice core

1. Introduction

The Greenland and Antarctic ice sheets are rapidly losing their ice mass (Mouginot *et al.*, 2019; Rignot *et al.*, 2019). There is urgent need to understand the mechanism of ice sheet mass loss because of its contribution to sea level rise. Accelerated ice flow to the oceans is one of the major causes of rapid mass loss (Mouginot *et al.*, 2019; Rignot *et al.*, 2019). To understand ice flow dynamics, it is important to investigate ice deformation mechanisms in ice sheets. Ice sheets are composed of hexagonal polycrystalline ice, which deforms mainly by dislocation glide on basal planes (Glen, 1955). This mechanism is regulated by c-axis orientation distribution (Azuma, 1994). Grain sizes and impurities might also affect deformation (Cuffey *et al.*, 2000b; Goldsby and Kohlstedt, 1997, 2001; Jones and Glen, 1969; Saruya *et al.*, 2019). Therefore, to understand deformation mechanisms of ice sheets, it is important to study the effects of grain size and impurities on deformation, as well as the mechanisms controlling c-axis orientation distribution and grain size in ice sheets.

Ice formed during glacial periods (hereafter referred to as glacial ice) deforms at a much higher rate than ice formed during interglacial periods (Dahl-Jensen and Gundestrup, 1987; Paterson, 1991). The higher deformation

rate of glacial ice has been reported to be associated with c-axis orientation distribution, grain size and/or higher impurity concentration (Dahl-Jensen and Gundestrup, 1987; Paterson, 1991), although exact mechanisms are yet unknown. Glacial ice also shows large variability in deformation rate. It usually contains light-scattering cloudy layers, which can be distinguished easily visually from their adjacent layers, which are clear (*e.g.*, "cloudy bands," described in Faria *et al.*, 2010; Faria *et al.*, 2018; Gow and Williamson, 1976; Jansen *et al.*, 2016; Miyamoto *et al.*, 1999; Svensson *et al.*, 2005). Compared with clear ice, cloudy bands have finer grain sizes (Faria *et al.*, 2010) and higher impurity concentrations (Svensson *et al.*, 2005). Miyamoto *et al.* (1999) reported higher deformation rates of ice containing cloudy bands. However, the mechanisms that lead to enhanced deformation in cloudy bands, and their relationships with grain size and impurity content remain unclear.

Analyses of microstructures (*e.g.*, crystallographic orientation, grain size, grain shape, including what are often referred to as substructures—subgrain boundaries, slip bands and gradual change in crystal orientations) of ice from polar ice sheets provide us with information about deformation mechanisms as well as the related processes of recovery and recrystallization (Faria *et al.*, 2010; Faria *et al.*, 2014a, 2014b; Faria *et al.*, 2018; Gow and Williamson, 1976; Hamann *et al.*, 2007; Jansen *et al.*, 2016; Kipfstuhl *et al.*, 2006; Miyamoto *et al.*, 1999; Montagnat *et al.*, 2014; Weikusat *et al.*, 2009; Weikusat *et al.*, 2011b; Weikusat *et al.*, 2017a, 2017b). Although grain size and c-axis orientation distribution in cloudy bands have been studied (Gow and Williamson, 1976; Miyamoto *et al.*, 1999), little is known about the substructures of cloudy bands (Weikusat *et al.*, 2009). Typical sizes of grains and sub-strucures in polar ice samples are several mm and $100\,\mu$ m to 1 mm, respectively (*e.g.*, Faria *et al.*, 2014a, 2014b; Fig. 5 in Kipfstuhl *et al.*, 2006). Misorientation angles of grain boundaries are less than 5° (Weikusat *et al.*, 2011b). To investigate substructures in polar ice samples, it is necessary to measure substructures with high spatial resolution and angular accuracy in large areas.

Conventional methods for analysing ice microstructure have several shortcomings. For example, an auto-mated fabric analyser can determine c-axis orientations in a thin section (approximately 10×10 cm) with an angular accuracy of approximately 1° (Wang and Azuma, 1999) and a spatial resolution of approximately $2.8\,\mu$m (Peternell *et al.*, 2011), but is unable to measure a-axis orientation. Using optical microscopy, grain boundaries and subgrain boundaries can be imaged with a spatial resolution of $3\,\mu$m for a similar sample area (approximately 10×10 cm), but misorientation angles of the subgrain boundaries cannot be measured (Kipfstuhl *et al.*, 2006; Weikusat *et al.*, 2009). An X-ray diffraction method can measure both c- and a-axis orientations and detect misorientation angles at subgrain boundaries with a reported accuracy of 0.5° (Miyamoto *et al.*, 2011).

However, substructures in polar ice sheets are of the order of $100\,\mu$m (*e.g.*, Fig. 5 in Kipfstuhl *et al.*, 2006) and are therefore not detected sufficiently using this method, which has a spatial resolution of 0.2 mm (Miyamoto *et al.*, 2011).

The electron backscatter diffraction (EBSD) technique, performed in a scanning electron microscope (SEM) provides both c- and a-axis orientation measurements with high angular accuracy (0.5° to 1°) and spatial resolution (several tens of nanometres; Humphreys, 2001; Humphreys and Brough, 1999; Humphreys *et al.*, 1999; Krieger Lassen, 1996). Although several research groups have analysed ice samples using a cryogenic SEM equipped with EBSD (cryogenic SEM/EBSD system) (Baker *et al.*, 2005; Baker *et al.*, 2007; Chauve *et al.*, 2017; Iliescu *et al.*, 2004; Montagnat *et al.*, 2015; Obbard *et al.*, 2006; Piazolo *et al.*, 2008; Prior *et al.*, 2012; Prior *et al.*, 2015; Qi *et al.*, 2017; Weikusat *et al.*, 2011a; Weikusat *et al.*, 2017b), they all employed slightly different instruments and different methods. Furthermore, while the spatial resolution and the angular error of EBSD measurements have been reported previously (*e.g.*, Humphreys *et al.*, 1999; Krieger Lassen, 1996; Weikusat *et al.*, 2011a), studies on orientation gradients (gradual changes in orientation in a grain) are limited for samples with grain sizes of several mm (Obbard *et al.*, 2006). Previous studies on angular accuracies of EBSD have focussed on smaller grain sizes (~$100\,\mu$m; *e.g.*, Humphreys *et al.*, 2001). In this study, we optimized a cryogenic SEM/EBSD system installed at the National Institute of Polar Research in Japan and we designed a sample preparation method to analyse ice samples. We assessed orientation gradients measured in our instrument using annealed artificial ice to analyse intragranular misorientations in polar ice samples. We analysed microstructures of glacial ice from a cloudy band and an adjacent clear layer from a shallow section of glacial ice in the Greenland Ice Sheet. In this paper, we discuss the differences between the cloudy band and its adjacent clear layer in terms of their microstructure.

2. Methods

2.1 Cryogenic ESEM/EBSD system

We used an environmental SEM (ESEM, Quanta 450 FEG; Thermo Fisher Scientific, Inc., Materials and Structural Analysis Division, Hillsboro, OR, USA), equipped with an EBSD detector (HKL NordlysNano; Oxford Instruments, plc, Abingdon, UK) and a Cryo-SEM preparation system (PP3010T; Quorum Technologies, Lewes, UK) (Fig. 1). The cryogenic ESEM/EBSD system has two cold stages: one within the ESEM chamber and the other in the preparation chamber used to transfer the sample into the ESEM chamber. Circulating dry nitrogen gas cooled by liquid nitrogen can lower the temperature of the cold stages to $-190\,℃$. An ice sample was prepared in our cold laboratory and transferred to the preparation deck (Fig. 1). Following transfer to the
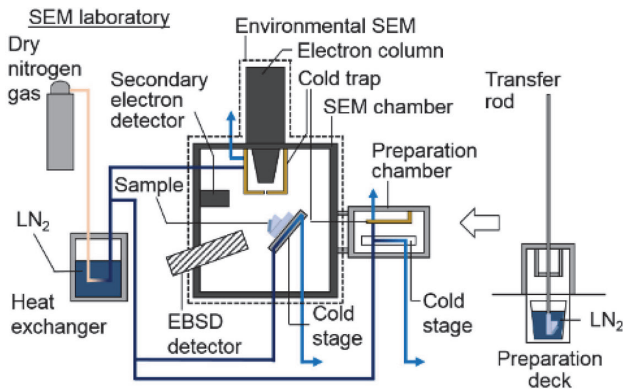
Fig. 1.   The cryogenic ESEM/EBSD system used in this study. The environmental scanning electron microscope (Environmental SEM; dark grey) has an electron back-scatter diffraction (EBSD) detector and a Cryo-SEM preparation system (which contains two cold stages, two cold traps, a preparation chamber, a preparation deck, a transfer rod and a heat exchanger). Note: LN_2 stands for liquid nitrogen.
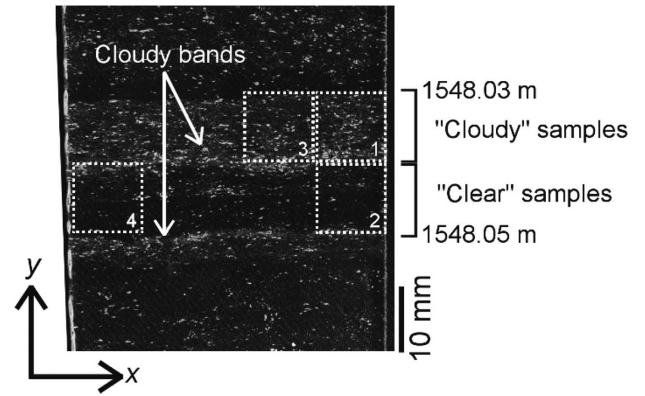

Fig. 3.   Locations of samples used in this study for electron backscatter diffraction mapping with respect to ice section from the North Greenland Eemian Ice Drilling (NEEM) ice core. Samples 1 and 3 originated from a cloudy band at depths of 1548.03–1548.04 m. Samples 2 and 4 originated from an adjacent clear layer at depths of 1548.04–1548.05 m.
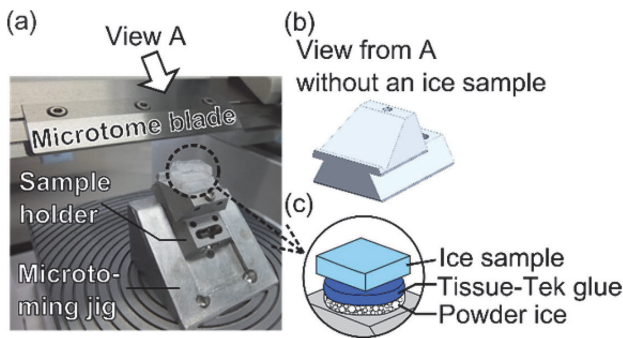

Fig. 2.   (a) Sample holder with 35° pre-tilt and jig used for polishing ice samples using a microtome. (b) Front view of sample holder without sample. (c) Schematic illustration of sample on holder.

preparation chamber, a transfer rod inserted the sample into the ESEM chamber. During sample transfer from the cold laboratory to the preparation chamber, liquid nitrogen kept the sample cold to avoid melting and condensation. This procedure is similar to that of Weikusat *et al.* (2011a). The procedure and time needed for our system are summarised in Appendices 1 and 2.

During EBSD analysis, tilting of the sample surface at an angle of 70° with respect to the horizontal plane is necessary to obtain diffraction patterns (called Kikuchi patterns) from backscattered electrons (Engler and Randle, 2009). We made a sample holder from aluminium alloy (JIS A7000 series) with a pre-tilt of 35° (Fig. 2). Using this holder, tilting of the cold stage to 35° ensured a sample tilt of 70°. The typical working distance was 20 mm, and the distance between the sample and the EBSD detector was 6–16 mm.

2.2   Samples

We made artificial ice samples with equiaxed grains and random crystal orientation distributions using the phase transition method (*e.g.*, Hamann *et al.*, 2007; Prior *et al.*, 2012) to evaluate the spatial resolutions and angular errors of our cryogenic EBSD system (Appendices 3 and 4, Section 2.4). Ultrapure water (electrical conductivity: ~$5.6 \times 10^{-6}\,S\,m^{-1}$) was frozen slowly, and ice phase was changed from ice I_h to ice II and back again to ice I_h by adjusting pressure. Prior annealing of samples at $-30℃$ for four years or more released any strain.

We analysed ice core samples retrieved by the North Greenland Eemian Ice Drilling (NEEM) project (NEEM community members, 2013). The NEEM drilling site is located at an ice ridge in the Greenland Ice Sheet (77.45° N, 51.06°W, surface elevation 2450 m, mean annual temperature $-29℃$, accumulation 0.22 m-ice equivalent per year; NEEM community members, 2013). We selected glacial ice samples from a depth of 1548 m, corresponding to an age of 19,200 years before present (Rasmussen *et al.*, 2013). This sample is from a shallow section of the glacial ice in the NEEM ice core (1419–2207 m). We analysed ice samples from a cloudy band and its adjacent clear layer in the sample.

Prior to EBSD mapping, we cut three sections (approximately 90 mm × 46 mm each) from the same depth interval (1547.99–1548.08 m) containing both cloudy bands and clear layers. We used two of the sections for grain size and c-axis orientation distribution measurements and the third section for EBSD mapping. We performed grain boundary mapping using an optical microscope (BX 51; Olympus Corp., Tokyo, Japan) (Kipfstuhl *et al.*, 2006; Weikusat *et al.*, 2009). We traced the boundaries manually and calculated the mean grain sizes using image processing software (Stream; Olympus Corp.). To measure c-axis orientation distributions in large areas, we used an automated fabric analyser (G50 Fabric Analyser; Russell-Head Instruments, Melbourne,

Australia). We selected four samples from the third section for EBSD mapping. Two samples were from a cloudy band and the other two samples were from the adjacent clear layer (Fig. 3). Before the samples were analysed in the ESEM, we mapped the grain and subgrain boundaries using an optical microscope (Appendix 1).

For EBSD analysis, an ice sample, typically with an area of $10\,mm \times 10\,mm$ and thickness of 5 mm, was cut in the cold laboratory ($-20°C$) with a bandsaw and fixed on to the sample holder using powder ice and a mixture of ultrapure water and cryogenic adhesive material (Tissue-Tek Optimum Cutting Temperature formulation, Sakura Finetek Japan, Co., Ltd, Tokyo, Japan), following Kitahara *et al*. (2016) (Appendix 1). We adopted this method to avoid cracking or detaching of the ice sample when submerged into liquid nitrogen (Section 2.1). Previous studies used water to fix an ice sample onto a holder or melted the bottom of an ice sample and refroze it to the holder (*e.g.*, Weikusat *et al*., 2011a; Prior *et al*., 2015); however, our trials of these methods often failed. We made powder ice by spraying ultrapure water into liquid nitrogen. The weight ratio of Tissue-Tek to water was roughly between 0.5 and 0.7.

We polished the samples with a microtome to ensure the sample surface was flat and smooth. Depending on the quality of the surface, sample surfaces were further sublimated in a cold room at $-20°C$ for up to 3 hours to make them smoother, and to remove small ice particles produced by microtoming (Appendix 1, details of sublimation-etching are described in Kipfstuhl *et al*. (2006) and Weikusat *et al*. (2009)). We designed a jig, which could attach to the sample holder, to polish samples fixed on to the holder (Fig. 2). This jig allowed us to observe the samples both in the ESEM and in the optical microscope without remounting them (Appendix 1).

2.3 ESEM/EBSD operation and data acquisition/processing

The optimum conditions for EBSD mapping were as follows: temperatures of the cold stage and trap were $-150°C$ and $-190°C$, respectively; chamber pressure was 10 Pa (Appendix 2). The chamber pressure was regulated using dry nitrogen gas, as used by Prior *et al*. (2015). To achieve best mapping efficiency, accelerating voltage of 30 kV and beam current of 9.2 nA (for a spot size of 6.0) or ≥ 30 nA (for a spot size of 7.0) were used.

We acquired Kikuchi patterns and indexed them using the software AZtec® (Oxford Instruments) under the conditions shown in Table 1. We created crystallographic data for theoretical Kikuchi patterns using the software Twist (Oxford Instruments) from the positions of oxygen atoms in the crystal structure of ice-I_h (Fletcher, 1970; Kuhs and Lehmann, 1986; Röttger *et al*., 1994). Initial indexing rates were between 79 % and 99 % for all data. Data were reanalysed when indexing rates were below 90 %. We analysed the indexed data using the software Channel 5 (Tango, Mambo, Data Manager, and

Table 1.   Conditions for acquiring and indexing Kikuchi patterns and crystallographic information for ice-I_h.

Binning	4×4 (336 × 256 pixels from full size of 1344 × 1024 pixel-charge coupled device)
Gain	High
Frame averaging[1]	5 to 10 frames
Exposure time[1]	2 to 12 ms
Reflectors	52
Band detection mode	Edge
Number of bands	10 to 12
Hough resolution	60 to 120
Crystallographic information of ice-I_h (oxygen atom)	Space group[2] : $P6_3/mmc$ Coordinates[2]: (x, y, z) $\pm(1/3, 2/3, z_o)$ $\pm(2/3, 1/3, z_o + 1/2)$ Wyckoff letter[3]: f Lattice constants[4]: $a = 4.51808\ m^{-10}$, $c = 7.35612\ m^{-10}$

Notes: [1] The resulting acquisition rate is 3.9–8 Hz. Crystallographic information is obtained from [2] Fletcher (1970), [3] Kuhs and Lehmann (1986) and [4] Röttger *et al*. (1994).

Map Stitcher; Oxford Instruments) (Appendix 1).

The EBSD mapping of the NEEM ice samples used a step size of $50\,\mu$m (Section 2.4). We displayed the c- and a-axis orientation distributions as equal area projections in the lower hemisphere on pole figures. To compare distributions quantitatively, the M-index, which ranges between 0 (random) and 1 (single crystal), was used (Skemer *et al.*, 2005) (Appendix 1). In both cloudy sample 1 and clear sample 2 (Fig. 3), the sample surface was imaged as two adjacent areas that could be stitched together using Map Stitcher. We removed those pixels not indexed or misindexed and replaced them based on interpolation using data from six adjacent pixels. We calculated averaged map values using the Advanced Kuwahara filter with a window size of 3×3 or 5×5 pixels (Appendix 1).

2.4 Spatial resolutions and angular accuracies

The spatial resolutions of our ESEM/EBSD system were assessed following Weikusat *et al.* (2011a) and found to be 0.6 and $1.8\,\mu$m for the direction parallel to the sample tilt axis (x-direction) and the direction perpendicular to it, respectively (Appendix 3). The spatial resolution of our cryogenic ESEM/EBSD system is sufficient to analyse substructures in ice from ice sheets, which have typical sizes of $100\,\mu$m to 1 mm (*e.g.*, Fig. 5 in Kipfstuhl *et al.*, 2006).

The misorientation angle between two lattice orientations is defined as the minimum angle by which one lattice orientation needs to be rotated to coincide with the other (*e.g.*, Engler and Randle, 2009). There are two methods for estimating misorientation errors in the EBSD system: (1) misorientation angles between neighbouring pixels and (2) orientation gradients, which represent gradual changes in orientation with respect to a reference point in the sample, expressed as angle per length. The errors of misorientation angles between neighbouring pixels were 0.6°–0.8° for all step sizes analysed (Appendix 4). These values are smaller than the misorientation angles characterising grain boundaries in ice (3°–5°; Weikusat *et al.*, 2011b), confirming that our EBSD analysis can identify ice substructures.

To detect a small orientation gradient within an ice crystal, we assessed the orientation change induced by our cryogenic ESEM/EBSD system. While the orientation change induced by our cryogenic ESEM/EBSD system is less than 1° at 100× magnification using software AZtec® (corresponding to an area of approximately 0.9 mm× 0.6 mm), the errors at lower magnification (for larger sample areas) are unknown. To assess the error induced by our system for large ice samples (approximately 10 mm×10 mm), we analysed a strain-free annealed artificial ice sample (approximately 8 mm×7 mm) containing two grains using step sizes of 50 and $100\,\mu$m.

3. Results

3.1 Error in orientation gradient estimated using annealed artificial ice

Figure 4 (a) shows a textural component map of the sample, while Fig. 4 (b) shows the variations of misorientation angles along profile lines running from the top to the bottom near the centre (lines B–B′ and C–C′) and near the outer edges (lines A–A′ and D–D′) of the sample. In both grains, misorientation angles show monotonic increases near the sides and saddle-shaped variations near the centre. To confirm that these misorientation angle variations result from our cryogenic ESEM/EBSD system and are not intrinsic to the sample, the sample was rotated anticlockwise by 90° and reanalysed (i.e., in this case, the 'top' of the sample in Fig. 4 (a) is now on the 'left'). Figure 4 (c) shows the variations of misorientation angles along profile lines near the centre (lines B–B′ and C–C′) from the first and second mapping. Although the same area of the same sample was analysed, misorientation angle variations were clearly different, suggesting that these variations are an artefact induced by the configuration of our cryogenic ESEM/EBSD system.

We evaluated the impact of this error on orientation gradients at grain-size scale (*i.e.*, mm-scale). Using least squares linear regression to relate misorientation angles to length, we calculated average regression slopes and standard deviations of misorientation angles of different profile lines on the annealed artificial ice sample (Table 2), and we found a maximum orientation gradient of $4\times10^{-4}\,°\mu$m^{-1} in our cryogenic ESEM/EBSD system. This was determined from line A–A′ using $[\text{OG}_{\text{GS}}]_{\text{max}}+2\sigma$, where $[\text{OG}_{\text{GS}}]_{\text{max}}$ denotes the maximum regression slope. This value is consistent with an orientation gradient (1.07° at 2 mm, namely $5.35\times10^{-4}\,°\mu$m^{-1}) reported by Obbard *et al.* (2006), using GISP2 (Greenland Ice Sheet Project 2) ice core.

In addition to the general monotonic increase and saddle-shaped variation in misorientation angles at the grain-size scale (Fig. 4 (b) and (c)), misorientation angles also showed smaller-scale (~100 μm) variations. To evaluate these smaller-scale artefacts, 10-point moving averages of orientation gradients ($\text{OG}_{\text{10-point}}$) were calculated and averaged ($[\text{OG}_{\text{10-point}}]_{\text{mean}}$) over each profile line (Table 2). The maximum $[\text{OG}_{\text{10-point}}]_{\text{mean}}+2\sigma$ value was $9\times10^{-4}\,°\mu$m^{-1} (along A–A′); this value was used as the maximum small-scale orientation gradient artefact of our cryogenic ESEM/EBSD system, and was taken into account during EBSD analysis with step sizes of 50 and $100\,\mu$m (Section 3.2.1).

3.2 NEEM ice core samples
3.2.1 Substructures

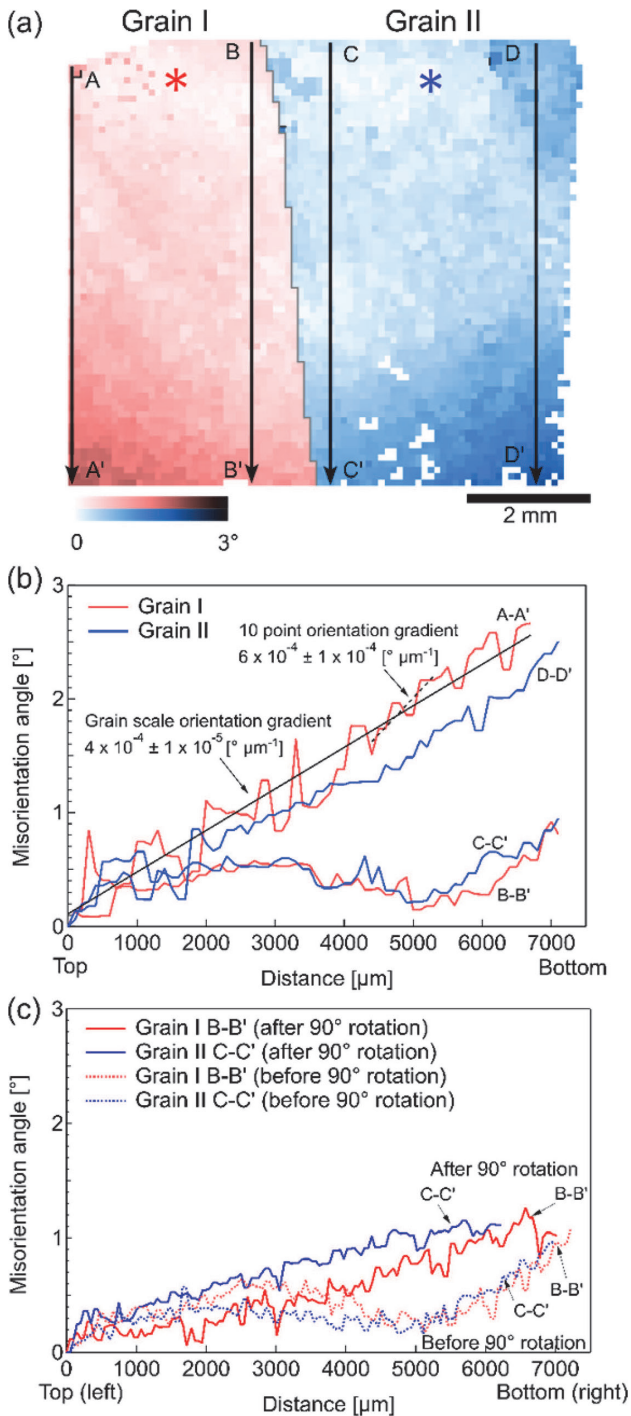Figure 5 shows optical microscope images and inverse pole figure maps of all analysed samples. We

Fig. 4. Observed orientation gradients in the annealed artificial ice sample. (a) Textural map showing orientation changes of up to 3° with respect to the orientation of the position marked with an asterisk in each grain (step size: 100 μm). (b) Misorientation angle profiles along lines (A–A′, B–B′, C–C′ and D–D′) in (a). (c) Misorientation angle profiles as in (b) before and after 90° rotation of the sample (step size: 50 μm). All data were averaged using the Advanced Kuwahara filter with a window size of 3×3 pixels.

removed regions of the inverse pole figure maps stitched together or not acquired and regions that displayed possible artefacts from data averaging, as shown in black in Fig. 5 (b) and (d). We defined grain and subgrain boundaries based on comparison of optical microscope images and misorientation data derived from EBSD mapping. We regarded sharp thick lines in the optical microscope images as grain boundaries and irregular thin lines as subgrain boundaries (*e.g.*, Kipfstuhl *et al.*, 2006; Weikusat *et al.*, 2009). Most grain boundaries in the optical microscope images coincided with misorientation angles greater than 4° (black lines) in the inverse pole figure maps. Likewise, most subgrain boundaries in the optical microscope images coincided with misorientation angles of 0.8°–4° (grey lines). Therefore, we regarded misorientations with angles greater than 4° as grain boundaries, and misorientations with angles of 0.8°–4° as subgrain boundaries. These results are consistent with misorientation angles of grain and subgrain boundaries derived using an X-ray diffraction method (Weikusat *et al.*, 2011b). We calculated subgrain boundary densities for both cloudy and clear ice samples by dividing the total length of subgrain boundaries in each map by the total area that was analysed. We calculated the total length of the subgrain boundaries by multiplying the step size of 50 μm with the number of misorientations with angles between 0.8° and 4° in all analysed areas (Appendix 1).

We calculated the misorientation angles between the average orientation of a grain and the pixels in each grain. The average of these values gives the grain orientation spread, which has been used as a measure of intragranular misorientation angles (Fig. 6). We used the software Tango to calculate grain orientation spreads for our EBSD data (Appendix 1). An artefact related to our cryogenic ESEM/EBSD system, which is proportional to the grain area analysed, affected the grain orientation spreads. To evaluate this artefact, we measured the grain orientation spreads of strain-free annealed ice and plotted the results against the analysed grain area (Fig. 7). We used least squares linear regression to relate grain orientation spread to analysed grain area. The regression line derived from annealed ice defined the baseline error related to the system artefact. For any sample, we considered values above the regression line as the grain orientation spreads.

We derived the orientation gradient of each grain using least squares linear regression of the misorientation angles measured along an arbitrary line across the grain (Fig. 8; Appendix 1). This can be a proxy for the number of dislocations piling up to form subgrain boundaries. On the basis of the error estimated in Section 3.1, we investigated the number of grains with orientation gradients greater than 9×10^{-4}°μm^{-1}. We analysed all grains larger than 10 pixels (500 μm). Sudden changes in misorientation angles at subgrain boundaries can indicate high orientation gradients (Fig. 8). Therefore, we considered that grains with misorientation angles larger than 0.8° contained subgrain boundaries and we analysed them separately.

Table 2. Errors in orientation gradients at grain-size scale and subgrain-size scale (derived from 10-point moving averages) in the environmental scanning electron microscope (ESEM)/electron backscattered diffraction (EBSD) system.

	Step size [μm]	OG_{GS} [° μm^{-1}]	$σ (OG_{GS})$ [° μm^{-1}]	$OG_{GS} + 2σ$ [° μm^{-1}]	$[OG_{10\text{-point}}]_{mean}$ [° μm^{-1}]	$[OG_{10\text{-point}}]_{mean} + 2σ$ [° μm^{-1}]
Grain I A-A'	100	$4 × 10^{-4}$	$1 × 10^{-5}$	$4 × 10^{-4}$	$4 × 10^{-4}$	$9 × 10^{-4}$
Grain II D-D'	100	$3 × 10^{-4}$	$8 × 10^{-6}$	$3 × 10^{-4}$	$3 × 10^{-4}$	$8 × 10^{-4}$
Grain I B-B'	100	$3 × 10^{-5}$	$9 × 10^{-6}$	$5 × 10^{-5}$	$8 × 10^{-5}$	$5 × 10^{-4}$
Grain II C-C'	100	$4 × 10^{-5}$	$9 × 10^{-6}$	$6 × 10^{-5}$	$7 × 10^{-5}$	$5 × 10^{-4}$
Grain I B-B' Horizontal	50	$2 × 10^{-4}$	$4 × 10^{-6}$	$2 × 10^{-4}$	$1 × 10^{-4}$	$6 × 10^{-4}$
Grain II C-C' Horizontal	50	$2 × 10^{-4}$	$3 × 10^{-6}$	$2 × 10^{-4}$	$1 × 10^{-4}$	$5 × 10^{-4}$
Grain I B-B' Vertical	50	$5 × 10^{-5}$	$7 × 10^{-6}$	$6 × 10^{-5}$	$1 × 10^{-4}$	$7 × 10^{-4}$
Grain II C-C' Vertical	50	$6 × 10^{-5}$	$6 × 10^{-6}$	$7 × 10^{-5}$	$1 × 10^{-4}$	$5 × 10^{-4}$

Note: OG, GS, $σ$ and $[OG_{10\text{-point}}]_{mean}$ denote orientation gradient, grain-size scale, standard deviation and mean 10-point moving averages of orientation gradient, respectively. Locations of profile lines A–A' to D–D' on Grains I and II are shown in Fig. 4.

3.2.2 *Comparison between the microstructures of cloudy and clear samples*

Mean grain sizes are smaller in the cloudy band (mean of 0.63 mm^2 calculated from 243 grains) than in the adjacent clear layer (mean of 1.4 mm^2 calculated from 220 grains) (Fig. 5; Table 3). Subgrain boundary density in the cloudy samples ($1.3×10^3$ m^{-1}) is five times that in the clear samples ($2.5×10^2$ m^{-1}; Fig. 5; Table 3) for misorientation angles of 0.8°–4°. Similarly, if we considered misorientation angles down to 0.4° from averaged map data (Appendix 4), we obtained the same conclusion that subgrain boundary density in the cloudy samples is higher than in the clear samples. As we found a small number of grain boundaries with misorientation angles below 4° and subgrain boundaries with misorientation angles above 4°, we needed to confirm that we could obtain the same conclusion for different thresholds of the misorientation angle used to distinguish subgrain boundaries from grain boundaries. We calculated subgrain boundary densities for threshold misorientation angles of 3° and 5°, following the findings of Weikusat *et al.* (2011b). The difference in the subgrain boundary densities was small: subgrain boundary densities for thresholds 3° and 5° were $1.2×10^3$ and $1.3×10^3$ m^{-1}, respectively, in the cloudy samples and $2.5×10^2$ and $2.6×10^2$ m^{-1}, respectively, in the clear samples. The presence of a very large grain in clear sample 2 reduced the subgrain boundary density (Fig. 5 (c) and (d)); however, its presence did not change our result markedly. If we excluded the large grain from our analysis, then the subgrain boundary density (with misorientation angles of 0.8°–4°) would be $3.8×10^2$ m^{-1}.

C-axis orientation distributions show single maxima in both cloudy and clear samples. A-axis orientations show uniform distribution in the horizontal plane with no notable differences between cloudy and clear samples (Fig. 9). Cloudy and clear samples exhibit similar M-indices (0.61 and 0.69 for cloudy and clear samples, respectively, Table 3). C-axis orientation distributions over larger sections using a fabric analyser confirmed the results of EBSD measurements carried out on smaller samples (Table 3).
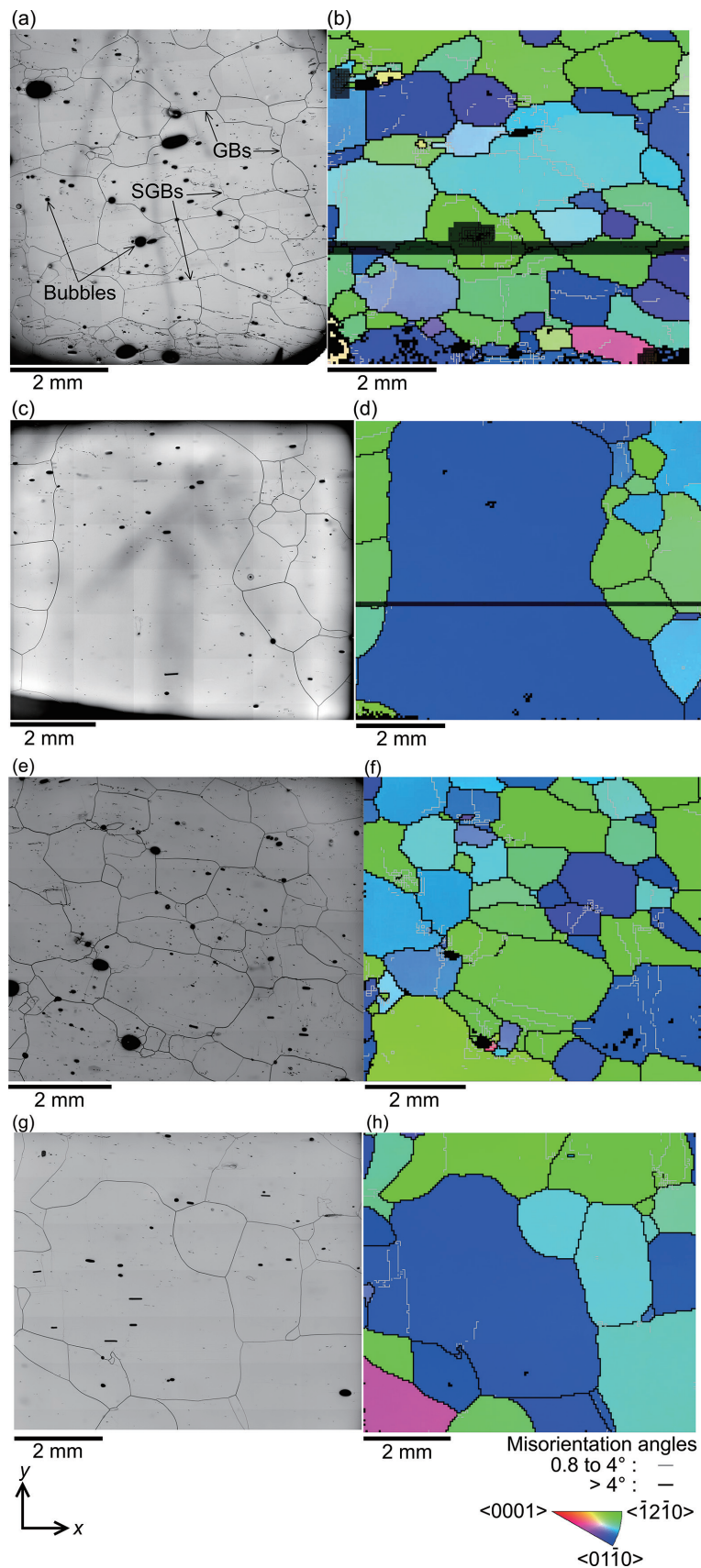
Fig. 5. Optical microscope images (images on the left) and inverse pole figure (IPF) maps from electron backscatter diffraction (EBSD) data (diagrams on the right; crystal orientations are given with respect to the direction that is perpendicular to the sample surface) for (a) (b) sample 1 (cloudy), (c) (d) sample 2 (clear), (e) (f) sample 3 (cloudy) and (g) (h) sample 4 (clear). In (b) and (d), black areas indicate regions of IPF maps stitched together or not acquired and regions that displayed possible artefacts from data averaging. Different aspect ratios in optical microscope images and IPF maps reflect incomplete tilt corrections on the EBSD measurements. Arrows visible in optical microscope images (a, c) were drawn on the glued surface of the samples to indicate the top of the samples.

Grain orientation spreads in both cloudy and clear samples are considerably higher than in strain-free annealed ice, suggesting the existence of intragranular misorientations in glacial ice samples. We used the least squares linear regression line derived from annealed ice to define the baseline error related to the artefact from our system (Fig. 7). Values of grain orientation spread of both cloudy and clear samples lie above the regression line, indicating the existence of a large number of intragranular misorientation angles that are larger than any measurement error.

The percentage of the total number of grains with orientation gradients that are larger than the estimated error induced by the system (estimated to be $9 \times 10^{-4}\,°\mu m^{-1}$ in Section 3.1) is markedly higher in the cloudy samples (31 out of 77 grains leading to a percentage of 40%) than in the clear samples (2 out of 27 grains leading to a percentage of 7%) (Table 3). Grains with subgrain boundaries can have high orientation gradients related to sudden orientation changes at subgrain boundaries (Fig. 8); however, in the cloudy samples, we detected large orientation gradients in grains with and without subgrain boundaries. Eighteen out of 77 grains in the cloudy samples contain subgrain boundaries, while 5 out of 27
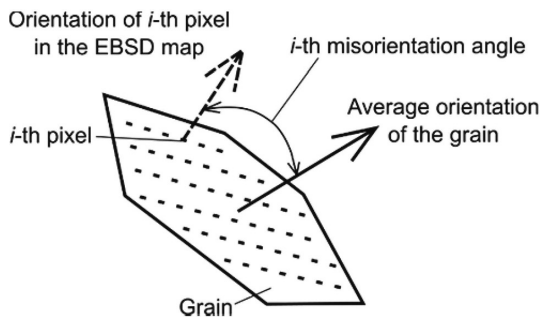
grains in the clear samples contain subgrain boundaries. For grains with subgrain boundaries, the percentage of grains that have orientation gradients larger than the estimated error is 61% in the cloudy samples and 0% in the clear samples. Likewise, for grains without subgrain boundaries, the percentage is 34% in the cloudy samples and 9% in the clear samples.

4. Discussion

Miyamoto *et al.* (1999) reported that ice samples containing cloudy bands from the last glacial period obtained by the Greenland Ice Core Project (GRIP) exhibited a deformation rate that was 67 times that of ice with random c-axis orientations. Difference in c-axis orientations can explain only 5 of the 67-fold difference (Azuma, 1995). Miyamoto *et al.* (1999) also reported inhomogeneous deformation in the samples containing
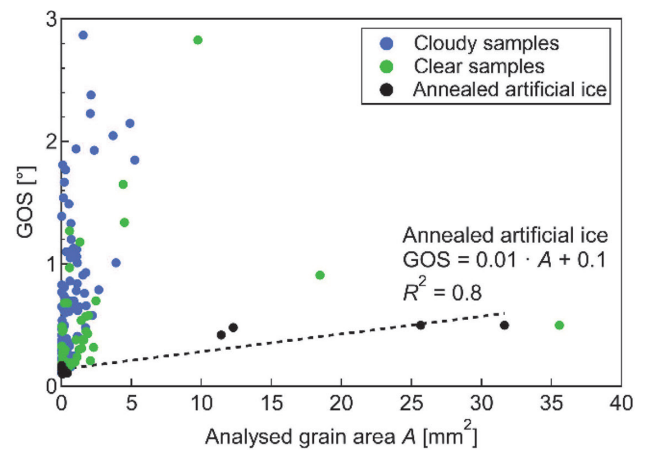
Fig. 7. Grain orientation spreads (GOSs) in the North Greenland Eemian Ice Drilling (NEEM) and artificial ice samples. Least squares linear regression line from annealed ice represents a baseline for removing errors from the electron backscatter diffraction system. Therefore, only GOS values above the regression line were used.

Fig. 6. Schematic illustration of a misorientation angle between the average orientation of a grain and an orientation of the *i*-th pixel, used for calculation of grain orientation spread.
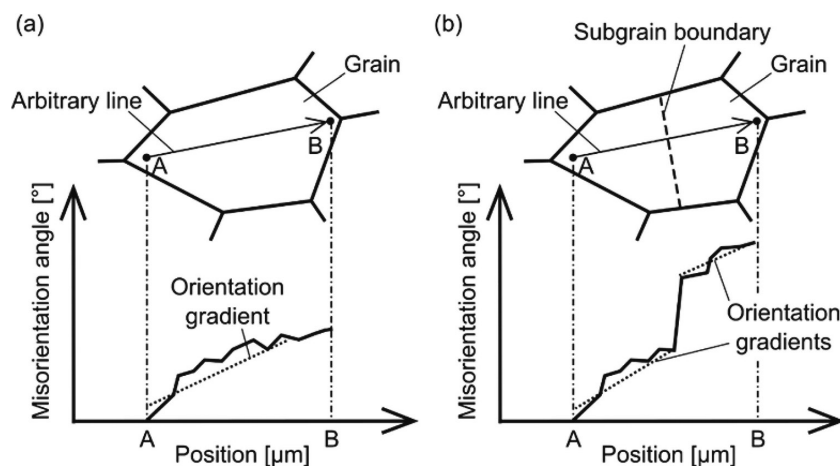
Fig. 8. Schematic illustrations showing calculation of orientation gradients in (a) a grain without subgrain boundaries and (b) a grain with a subgrain boundary.

Table 3. Microstructures of North Greenland Eemian Ice Drilling (NEEM) ice samples

Parameter (analysis method)	Cloudy band samples	Clear layer samples
Mean grain size (OM)	0.63 mm²	1.4 mm²
Schmid factor: mean ± standard deviation (FA)	0.40 ± 0.11	0.42 ± 0.09
M-index: mean ± standard deviation (EBSD)	0.61 ± 0.014	0.69 ± 0.059
Subgrain boundary density: mean ± standard deviation (EBSD)	$1.3 \times 10^3 \pm 1.6 \times 10^2 \, \text{m}^{-1}$	$2.5 \times 10^2 \pm 1.6 \times 10^2 \, \text{m}^{-1}$
Number fraction of grains with orientation gradient $> 9 \times 10^{-4} \, °$ μm^{-1} (EBSD)	40%	7%

Notes: OM, FA and EBSD denote optical microscopy, fabric analyser and electron backscatter diffraction, respectively. The M-indices and subgrain boundary densities were derived from EBSD measurements; for each sample type (cloudy band and clear layer), mean and standard deviation obtained from the two samples of each type are shown. Schmid factor is a measure of orientation dependency of deformation for each grain. For ice, it is defined by $\cos\alpha\sin\alpha$, where α is the angle between the c-axis orientation and stress-axis direction (Azuma, 1995). Table shows mean Schmid factors for $\alpha = 45°$, which was used in the experiment by Miyamoto *et al.* (1999).
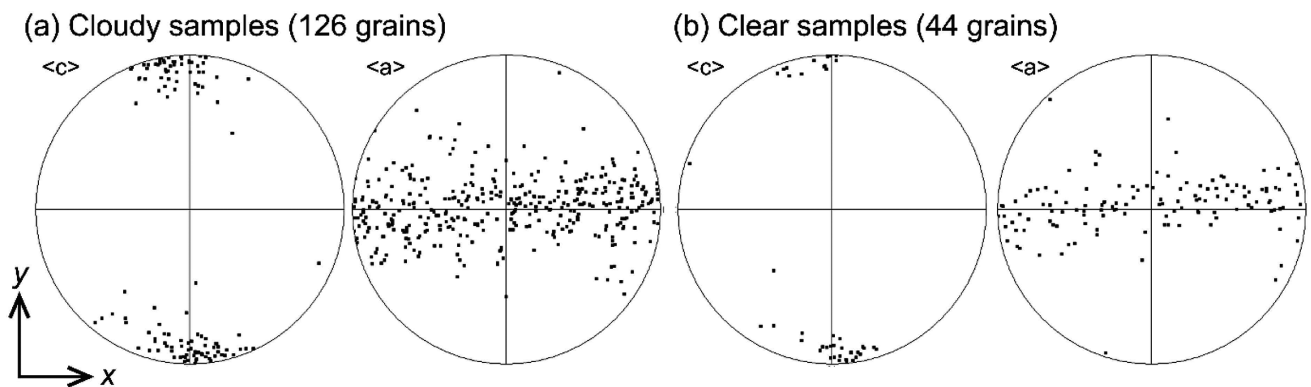

Fig. 9. C- and a-axis orientation distributions shown as equal area projections in the lower hemisphere on pole figures (PFs). For each grain, the orientation of a pixel chosen at random represents crystal orientation. (a) Combination of data from both cloudy samples (samples 1 and 3, 126 grains) and (b) combination of data from both clear samples (samples 2 and 4, 44 grains).

cloudy bands and small differences in c-axis orientation distributions with weak single-maxima in one of their cloudy samples. We recognise that the deformation mechanisms might have differed between the cloudy bands and the clear ice; however, previous studies have not carried out detailed analyses of substructures in clear and cloudy ice.

For our samples from the NEEM ice core, we found little difference between cloudy and clear ice in terms of their c- and a-axis orientation distributions. C-axis orientation distribution, which is associated with basal dislocation glide, is unlikely to be the primary cause of high deformation rates in cloudy bands around 1548 m depth in the NEEM ice core. Non-basal dislocation glide, which has been suggested to be linked to a-axis orientation distribution (Llorens *et al.*, 2016a; Llorens *et al.*, 2016b; Llorens *et al.*, 2017; Miyamoto *et al.*, 2005), has

been observed in some NEEM samples (Weikusat *et al.*, 2017b). However, there is little difference between our cloudy and clear samples in terms of their a-axis orientation (Fig. 9; Table 3). Therefore, non-basal dislocation glide may also be unable to explain high deformation rates in cloudy bands around 1548 m depth in the NEEM ice core. We found high grain orientation spreads in both cloudy and clear samples thereby confirming that dislocation glide contributes to the deformation of both cloudy and clear ice, although there is little difference between our cloudy and clear samples in terms of their c- and a-axis orientation distributions and grain orientation spread.

Conversely, cloudy and clear ice samples have different subgrain boundary densities and orientation gradients. Thus, subgrain boundary densities and orientation gradients may be better measures of

intragranular misorientation. Higher subgrain boundary densities and higher ratios of grains with large orientation gradients in the cloudy band suggest that there are more dislocations in the cloudy band than in the clear layer, despite little difference between the two ice types in terms of their c- and a-axis orientation distributions. It is noteworthy that the cloudy band has large orientation gradients in grains without subgrain boundaries. These findings are important for understanding the causes of higher dislocation density in the cloudy band. As our samples are from a shallow section (1548 m) of the glacial ice in the NEEM ice core (1419–2207 m), which should have experienced less deformation than deeper ice, analyses of deeper sections of the NEEM glacial ice should be performed to investigate the contrasts in dislocation density between cloudy bands and clear layers in much-deformed ice.

Enhanced deformation of cloudy bands (Miyamoto *et al.*, 1999) could be caused by fine grain size, which has been observed in this and previous studies, and/or high impurity concentrations (Cuffey *et al.*, 2000a; Cuffey *et al.*, 2000b; Dahl-Jensen and Gundestrup, 1987; Goldsby and Kohlstedt, 1997, 2001; Paterson, 1991, Saruya *et al.*, 2019). However, the relative contribution of grain size and impurity effects is yet unknown, because impurities could affect both grain size (Alley *et al.*, 1986; Durand *et al.*, 2006; Paterson, 1991, Saruya *et al.*, 2019) and dislocation density/velocity (Jones and Gilra, 1973). Several steps are necessary to understand the causes of enhanced deformation of cloudy bands. First, contrasts in dislocation density between cloudy bands and clear layers need investigation as functions of grain size, impurity content and deformation history, based on in-depth analyses of microstructures and impurities in several ice cores from different sites. EBSD provides good proxies for dislocation density such as subgrain boundary density and orientation gradient, as shown in this work. Two-dimensional orientation gradients should also be analysed for better understanding of the distribution and evolution of dislocations during deformation. Second, deformation experiments and microstructural analyses on samples before and after the experiments could elucidate the change in dislocation density with increased strain, together with the evolution of grain size. Third, deformation experiments of artificial ice samples could confirm the causes of enhanced deformation of cloudy bands under controlled conditions (*e.g.*, Saruya *et al.*, 2019).

Although our study focussed on only one depth interval from the NEEM ice core, our results suggest that cryogenic ESEM/EBSD is a useful technique for the analysis of ice microstructure to understand the effects of dislocation, grain-size-sensitive creep and recrystallization processes in ice sheets. Application of the technique could also help improve our understanding of the higher deformation rate of glacial ice in ice sheets.

References

Alley, R., Perepezko, J. and Bentley, C. (1986): Grain growth in polar ice: I. Theory. *J. Glaciol.*, **32** (112), 415–424, doi:10.1017/s0022143000012120.

Azuma, N. (1994): A flow law for anisotropic ice and its application to ice sheets. *Earth Planet. Sci. Lett.*, **128** (3), 601–614, doi:10.1016/0012-821X (94)90173-2.

Azuma, N. (1995): A flow law for anisotropic polycrystalline ice under uniaxial compressive deformation. *Cold Reg. Sci. Technol.*, **23** (2), 137–147, doi:10.1016/0165-232X (94)00011-L.

Baker, I., Iliescu, D., Obbard, R., Chang, H., Bostick, B. and Daghlian, C.P. (2005): Microstructural characterization of ice cores. *Ann. Glaciol.*, **42** (1), 441–444, doi:10.3189/172756405781812853.

Baker, I., Obbard, R., Iliescu, D. and Meese, D. (2007): Microstructural characterization of firn. *Hydrol. Process*, **21** (12), 1624–1629, doi:10.1002/hyp.6725.

Bielska, K., Havey, D.K., Scace, G.E., Lisak, D., Harvey, A.H. and Hodges, J.T. (2013): High-accuracy measurements of the vapor pressure of ice referenced to the triple point. *Geophys. Res. Lett.*, **40** (23), 6303–6307, doi:10.1002/2013GL058474.

Chauve, T., Montagnat, M., Barou, F., Hidas, K., Tommasi, A. and Mainprice, D. (2017): Investigation of nucleation processes during dynamic recrystallization of ice using cryo-EBSD. *Philos. Trans. R. Soc., A.*, **375** (2086), doi:10.1098/rsta.2015.0345.

Cuffey, K., Conway, H., Gades, A., Hallet, B., Raymond, C. and Whitlow, S. (2000a): Deformation properties of subfreezing glacier ice: role of crystal size, chemical impurities, and rock particles inferred from in situ measurements. *J. Geophys. Res.: Solid Earth*, **105** (B12), 27895–27915, doi:10.1029/2000jb900271.

Cuffey, K.M., Thorsteinsson, T. and Waddington, E.D. (2000b): A renewed argument for crystal size control of ice sheet strain rates. *J. Geophys. Res.: Solid Earth*, **105** (B12), 27889–27894, doi:10.1029/2000JB900270.

Dahl-Jensen, D. and Gundestrup, N. (1987): Constitutive properties of ice at Dye 3, Greenland, *The Physical Basis of Ice Sheet*

Modelling (Proceedings of the Vancouver Symposium, August 1987). IAHS Publ. no. 170, 31–43.

Durand, G., Weiss, J., Lipenkov, V., Barnola, J.M., Krinner, G., Parrenin, F., Delmonte, B., Ritz, C., Duval, P., Röthlisberger, R. and Bigler, M. (2006): Effect of impurities on grain growth in cold ice sheets. *J. Geophys. Res.: Earth Surface*, **111** (F1), F01015, doi:10.1029/2005JF000320.

Engler, O. and Randle, V. (2009): *Introduction to texture analysis: macrotexture, microtexture, and orientation mapping*, 2 nd ed., CRC press, Boca Raton.

Faria, S.H., Freitag, J. and Kipfstuhl, S. (2010): Polar ice structure and the integrity of ice-core paleoclimate records. *Quat. Sci. Rev.*, **29** (1–2), 338–351, doi:10.1016/j.quascirev.2009.10.016.

Faria, S.H., Weikusat, I. and Azuma, N. (2014a): The microstructure of polar ice. Part I: Highlights from ice core research. *J. Struct. Geol.*, **61**, 2–20, doi:10.1016/j.jsg.2013.09.010.

Faria, S.H., Weikusat, I. and Azuma, N. (2014b): The microstructure of polar ice. Part II: State of the art. *J. Struct. Geol.*, **61**, 21–49, doi:10.1016/j.jsg.2013.11.003.

Faria, S.H., Kipfstuhl, S. and Lambrecht, A. (2018): *The EPICA-DML Deep Ice Core: A Visual Record*, Springer-Verlag GmbH Germany, Berlin, Germany.

Fletcher, N.H. (1970): *The Chemical Physics of Ice*, Cambridge University Press, Cambridge, doi: 10.1017/CBO9780511735639.

Glen, J.W. (1955): The creep of polycrystalline ice. *Proceedings of the Royal Society of London A: Mathematical, Physical and Engineering Sciences*, **228** (1175), 519–538.

Goldsby, D.L. and Kohlstedt, D.L. (1997): Grain boundary sliding in fine-grained ice I. *Scr. Mater.*, **37** (9), 1399–1406, doi:10.1016/s1359-6462(97)00246-7.

Goldsby, D.L. and Kohlstedt, D.L. (2001): Superplastic deformation of ice: Experimental observations. *J. Geophys. Res.: Solid Earth*, **106** (B6), 11017, doi:10.1029/2000jb900336.

Gow, A.J. and Williamson, T. (1976): Rheological implications of the internal structure and crystal fabrics of the West Antarctic ice sheet as revealed by deep core drilling at Byrd Station. *GSA Bulletin*, **87** (12), 1665–1677, doi:10.1130/0016-7606 (1976)87＜1665: RIOTIS＞2.0.CO;2.

Hamann, I., Weikusat, C., Azuma, N. and Kipfstuhl, S. (2007): Evolution of ice crystal microstructure during creep experiments. *J. Glaciol.*, **53** (182), 479–489, doi:10.3189/002214307783258341.

Hobbs, V.P. (1974): *Ice physics*, Oxford University Press, London.

Humphreys, F.J. (2001): Review grain and subgrain characterisation by electron backscatter diffraction. *J. Mater. Sci.*, **36** (16), 3833–3854.

Humphreys, F.J. and Brough, I. (1999): High resolution electron backscatter diffraction with a field emission gun scanning electron microscope. *J. Microsc.*, **195** (Pt 1), 6–9.

Humphreys, F.J., Huang, Y., Brough, I. and Harris, C. (1999): Electron backscatter diffraction of grain and subgrain structures — resolution considerations. *J. Microsc.*, **195** (3), 212–216, doi:10.1046/j.1365-2818.1999.00579.x.

Humphreys, F.J., Bate, P.S. and Hurley, P.J. (2001): Orientation averaging of electron backscattered diffraction data. *J. Microsc.*, **201** (1), 50–58, doi:10.1046/j.1365-2818.2001.00777.x.

Iliescu, D., Baker, I. and Chang, H. (2004): Determining the orientations of ice crystals using electron backscatter patterns. *Microsc. Res. Tech.*, **63** (4), 183–187, doi:10.1002/jemt.20029.

Jansen, D., Llorens Verde, M.G., Westhoff, J., Steinbach, F., Kipfstuhl, S., Bons, P.D., Griera, A. and Weikusat, I. (2016): Small-scale disturbances in the stratigraphy of the NEEM ice core: observations and numerical model simulations. *Cryosphere*, **10**, 359–370, doi:10.5194/tc-10-359-2016.

Jones, S.J. and Glen, J.W. (1969): The effect of dissolved impurities on the mechanical properties of ice crystals. *The Philosophical Magazine: A Journal of Theoretical Experimental and Applied Physics*, **19** (157), 13–24, doi:10.1080/14786436908217758.

Jones, S.J. and Gilra, N.K. (1973): X-ray topographical study of dislocations in pure and HF-doped ice. *The Philosophical Magazine: A Journal of Theoretical Experimental and Applied Physics*, **27** (2), 457–472, doi:10.1080/14786437308227420.

Kipfstuhl, S., Hamann, I., Lambrecht, A., Freitag, J., Faria, S.H., Grigoriev, D. and Azuma, N. (2006): Microstructure mapping: a new method for imaging deformation-induced microstructural features of ice on the grain scale. *J. Glaciol.*, **52** (178), 398–406, doi:10.3189/172756506781828647.

Kitahara, S., Desaki, J., Yoshii, A., Matsui, A., Morikawa, S. and Ezaki, T. (2016): Electron microscopic study of capillary network remodeling in the extensor digitorum longus muscle of normal adult rat. *Microscopy*, **65** (6), 508–516, doi:10.1093/jmicro/dfw040.

Krieger Lassen, N.C. (1996): The relative precision of crystal orientations measured from electron backscattering patterns. *J. Microsc.*, **181** (1), 72–81, doi:10.1046/j.1365-2818.1996.95376.x.

Kuhs, W.F. and Lehmann, M.S. (1986): The Structure of Ice-Ih, *In* Franks, F. (ed.), *Water Science Reviews 2: Crystalline Hydrates*, pp. 1–66, Cambridge University Press, Cambridge, doi: 10.1017/CBO9780511897504.001.

Llorens, M.-G., Griera, A., Bons, P.D., Lebensohn, R.A., Evans, L.A., Jansen, D. and Weikusat, I. (2016a): Full-field predictions of ice dynamic recrystallisation under simple shear conditions. *Earth Planet. Sci. Lett.*, **450**, 233–242, doi:10.1016/j.epsl.2016.06.045.

Llorens, M.-G., Griera, A., Bons, P.D., Roessiger, J., Lebensohn, R., Evans, L. and Weikusat, I. (2016b): Dynamic recrystallisation of ice aggregates during co-axial viscoplastic deformation: a numerical approach. *J. Glaciol.*, **62** (232), 359–377, doi:10.1017/jog.2016.28.

Llorens, M.-G., Griera, A., Steinbach, F., Bons, P.D., Gomez-Rivas, E., Jansen, D., Roessiger, J., Lebensohn, R.A. and Weikusat, I. (2017): Dynamic recrystallization during deformation of polycrystalline ice: insights from numerical simulations. *Philos. Trans. R. Soc., A.*, **375** (2086), doi:10.1098/rsta.2015.0346.

NEEM community members (2013): Eemian interglacial reconstructed from a Greenland folded ice core. *Nature*, **493** (7433), 489–494, doi:10.1038/nature11789.

Miyamoto, A., Narita, H., Hondoh, T., Shoji, H., Kawada, K., Watanabe, O., Dahl-Jensen, D., Gundestrup, N.S., Clausen, H.B. and Duval, P. (1999): Ice-sheet flow conditions deduced from mechanical tests of ice core. *Ann. Glaciol.*, **29** (1), 179–183, doi:10.3189/172756499781820950.

Miyamoto, A., Shoji, H., Hori, A., Hondoh, T., Clausen, H.B. and Watanabe, O. (2005): Ice fabric evolution process understood from anisotropic distribution of a-axis orientation on the GRIP (Greenland) ice core. *Ann. Glaciol.*, **42**, 47–52, doi:10.3189/172756405781812501.

Miyamoto, A., Weikusat, I. and Hondoh, T. (2011): Instruments and methods: Complete determination of ice crystal orientation using Laue X-ray diffraction method. *J. Glaciol.*, **57** (201), 103–110, doi:10.3189/002214311795306754.

Montagnat, M., Azuma, N., Dahl-Jensen, D., Eichler, J., Fujita, S., Gillet-Chaulet, F., Kipfstuhl, S., Samyn, D., Svensson, A. and Weikusat, I. (2014): Fabric along the NEEM ice core, Greenland, and its comparison with GRIP and NGRIP ice cores. *Cryosphere*, **8**, 1129–1138, doi:10.5194/tc-8-1129-2014.

Montagnat, M., Chauve, T., Barou, F., Tommasi, A., Beausir, B. and Fressengeas, C. (2015): Analysis of Dynamic Recrystallization of Ice from EBSD Orientation Mapping. *Front. Earth. Sci.*, **3** (81), doi:10.3389/feart.2015.00081.

Mouginot, J., Rignot, E., Bjørk, A.A., van den Broeke, M., Millan, R., Morlighem, M., Noël, B., Scheuchl, B. and Wood, M. (2019): Forty-six years of Greenland Ice Sheet mass balance from 1972 to 2018. *PNAS*, **116** (19), 9239–9244, doi:10.1073/pnas.1904242116.

Obbard, R., Baker, I. and Sieg, K. (2006): Using electron backscatter diffraction patterns to examine recrystallization in polar ice sheets. *J. Glaciol.*, **52** (179), 546–557, doi:10.3189/172756506781828458.

Paterson, W.S.B. (1991): Why ice-age ice is sometimes "soft". *Cold. Reg. Sci. Technol.*, **20** (1), 75–98, doi:10.1016/0165-232X

(91)90058-O.

Peternell, M., Russell-Head, D.S. and Wilson, C.J.L. (2011): A technique for recording polycrystalline structure and orientation during in situ deformation cycles of rock analogues using an automated fabric analyser. *J. Microsc.*, **242** (2), 181–188, doi:10.1111/j.1365-2818.2010.03456.x.

Piazolo, S., Montagnat, M. and Blackford, J.R. (2008): Substructure characterization of experimentally and naturally deformed ice using cryo-EBSD. *J. Microsc.*, **230** (3), 509–519, doi:10.1111/j.1365-2818.2008.02014.x.

Prior, D.J., Diebold, S., Obbard, R., Daghlian, C., Goldsby, D.L., Durham, W.B. and Baker, I. (2012): Insight into the phase transformations between ice Ih and ice II from electron backscatter diffraction data. *Scr. Mater.*, **66** (2), 69–72, doi:10.1016/j.scriptamat.2011.09.044.

Prior, D.J., Lilly, K., Seidemann, M., Vaughan, M., Becroft, L., Easingwood, R., Diebold, S., Obbard, R., Daghlian, C., Baker, I., Caswell, T., Golding, N., Goldsby, D., Durham, W.B., Piazolo, S. and Wilson, C.J. (2015): Making EBSD on water ice routine. *J. Microsc.*, **259** (3), 237–256, doi:10.1111/jmi.12258.

Qi, C., Goldsby, D.L. and Prior, D.J. (2017): The down-stress transition from cluster to cone fabrics in experimentally deformed ice. *Earth Planet. Sci. Lett.*, **471**, 136–147, doi:10.1016/j.epsl.2017.05.008.

Röttger, K., Endriss, A., Ihringer, J., Doyle, S. and Kuhs, W.F. (1994): Lattice constants and thermal expansion of H_2O and D_2O ice I_h between 10 and 265 K. *Acta Crystallogr.*, **B50** (6), 644–648, doi:10.1107/S0108768194004933.

Rasmussen, S.O., Abbott, P.M., Blunier, T., Bourne, A.J., Brook, E., Buchardt, S.L., Buizert, C., Chappellaz, J., Clausen, H.B., Cook, E., Dahl-Jensen, D., Davies, S.M., Guillevic, M., Kipfstuhl, S., Laepple, T., Seierstad, I.K., Severinghaus, J.P., Steffensen, J.P., Stowasser, C., Svensson, A., Vallelonga, P., Vinther, B.M., Wilhelms, F. and Winstrup, M. (2013): A first chronology for the North Greenland Eemian Ice Drilling (NEEM) ice core. *Clim. Past*, **9** (6), 2713–2730, doi:10.5194/cp-9-2713-2013.

Rignot, E., Mouginot, J., Scheuchl, B., van den Broeke, M., van Wessem, M.J. and Morlighem, M. (2019): Four decades of Antarctic Ice Sheet mass balance from 1979–2017. *PNAS*, **116** (4), 1095–1103, doi:10.1073/pnas.1812883116.

Saruya, T., Nakajima, K., Takata, M., Homma, T., Azuma, N. and Goto-Azuma, K. (2019): Effects of microparticles on deformation and microstructural evolution of fine-grained ice. *J. Glaciol.*, **65** (252), 531–541, doi:10.1017/jog.2019.29.

Skemer, P., Katayama, I., Jiang, Z. and Karato, S. (2005): The misorientation index: Development of a new method for calculating the strength of lattice-preferred orientation. *Tectonophysics*, **411** (1), 157–167, doi:10.1016/j.tecto.2005.08.023.

Svensson, A., Nielsen, S.W., Kipfstuhl, S., Johnsen, S.J., Steffensen, J.P., Bigler, M., Ruth, U. and Röthlisberger, R. (2005): Visual stratigraphy of the North Greenland Ice Core Project (NorthGRIP) ice core during the last glacial period. *J. Geophys. Res.: Atmospheres*, **110** (D2), doi:10.1029/2004JD005134.

Wang, Y. and Azuma, N. (1999): A new automatic ice-fabric analyzer which uses image-analysis techniques. *Ann. Glaciol.*, **29**, 155–162, doi:10.3189/172756499781821021.

Weikusat, I., Kipfstuhl, S., H. Faria, S., Azuma, N. and Miyamoto, A. (2009): Subgrain boundaries and related microstructural features in EDML (Antarctica) deep ice core. *J. Glaciol.*, **55** (191), 461–472, doi:10.3189/002214309788816614.

Weikusat, I., De Winter, D.A.M., Pennock, G.M., Hayles, M., Schneijdenberg, C.T.W.M. and Drury, M.R. (2011a): Cryogenic EBSD on ice: preserving a stable surface in a low pressure SEM. *J. Microsc.*, **242** (3), 295–310, doi:10.1111/j.1365-2818.2010.03471.x.

Weikusat, I., Miyamoto, A., Faria, S.H., Kipfstuhl, S., Azuma, N. and Hondoh, T. (2011b): Subgrain boundaries in Antarctic ice quantified by X-ray Laue diffraction. *J. Glaciol.*, **57** (201), 111–120, doi:10.3189/002214311795306628.

Weikusat, I., Jansen, D., Binder, T., Eichler, J., Faria, S.H., Wilhelms, F., Kipfstuhl, S., Sheldon, S., Miller, H., Dahl-Jensen, D. and Kleiner, T. (2017a): Physical analysis of an Antarctic ice core — towards an integration of micro- and macro-dynamics of polar ice. *Philos. Trans. R. Soc., A*, **375** (2086), doi:10.1098/rsta.2015.0347.

Weikusat, I., Kuiper, E.J.N., Pennock, G.M., Kipfstuhl, S. and Drury, M.R. (2017b): EBSD analysis of subgrain boundaries and dislocation slip systems in Antarctic and Greenland ice. *Solid Earth*, **8** (5), 883–898, doi:10.5194/se-8-883-2017.

Appendix 1.   Procedure of EBSD analysis

We performed EBSD analyses using the ESEM with a procedure summarised in Table 4.

Appendix 2.   Optimum condition of ESEM for EBSD of ice samples

To map ice sample surfaces with an ESEM, it is necessary to minimise sublimation and condensation (Iliescu *et al.*, 2004). Theoretically, when temperature and pressure lie on the sublimation curve, sublimation and condensation are in equilibrium (Fig. 10). In reality, in an ESEM system, temperature and pressure are not measured exactly at the ice surface; hence, most previous cryogenic EBSD studies of ice (Chauve *et al.*, 2017; Montagnat *et al.*, 2015; Obbard *et al.*, 2006; Prior *et al.*, 2012; Prior *et al.*, 2015; Qi *et al.*, 2017; Weikusat *et al.*, 2011a; Weikusat *et al.*, 2017b) have been carried out at a lower temperature and a higher chamber pressure than on the sublimation curve (Fig. 10). In addition to sublimation and condensation, electrical charging could also affect SEM observations (Iliescu *et al.*, 2004) because ice has low electrical conductivity (~10^{-7} S m^{-1}; Hobbs, 1974). Optimum temperature and pressure to minimise sublimation, condensation and electrical charging in our ESEM were −150℃ for the cold stage, −190℃ for the cold trap and 10 Pa for chamber pressure (Fig. 10); conditions achieved using dry nitrogen gas, as in Prior *et al.* (2015). Under optimal conditions, mapping of an ice sample can continue for several hours. Sometimes frost particles appeared on sample surfaces just after transfer and occasionally during EBSD mapping. In these cases, we allowed the surface to sublimate under controlled conditions by increasing the temperature of the cold stage to around −90℃ to remove the frost particles, as described in Weikusat *et al.* (2011a).

Appendix 3.   Assessment of spatial resolution

To assess the spatial resolution of EBSD on ice samples, line scan analyses were performed across grain boundaries in the strain-free annealed ice (Section 2.2), following Weikusat *et al.* (2011a). We counted the number of Kikuchi patterns with bands originating from two neighbouring grains, and calculated the spatial resolution by multiplying the number of the Kikuchi patterns by

Table 4. Procedure and time needed for EBSD analysis using the ESEM

Step	Time	Related section in the main text
The day before an EBSD experiment		
Installing cold stage to the SEM chamber	~10 min	
Pre-vacuuming ESEM and preparation chambers [1]	~12 h	
The day of an EBSD experiment		
Circulating dry nitrogen to the Cryo-SEM preparation system [2]	~1 h	
Cooling the cold stages and traps	~1 h	
Selecting and cutting an ice sample	~1 h	2.2
Fixing an ice sample to the holder	~30 min	2.2
Microtoming the ice sample	~1 h	2.2
Sublimation-etching of the sample surface	~3 h	2.2
Mapping grain and subgrain boundaries with optical microscopy	~10 min	2.2
Submersion of sample in liquid nitrogen in the cold laboratory	~10 min	2.1 and 2.2
Transferring the ice sample to ESEM chamber	~10 min	2.1
Frost removal by controlled sublimation	~10 min × several times depending on the ice surface condition	Appendix 1
EBSD mapping	~1 h (sample size 7 × 5 mm, step size 50 μm)	2.3
EBSD data analyses		
Re-indexing EBSD data (if necessary)	~1 h	2.3
Map stitching, treatment of data misindexed or not indexed and averaging the data	~30 min	2.3
Analysis of crystal orientation distributions	~30 min	2.3
Analysis of grain orientation spread	~30 min	3.2.1
Calculating subgrain boundary density	~30 min	3.2.1
Analysis of orientation gradient	~3 h	3.2.1

Notes:

[1] Pre-vacuuming can reduce the amount of water vapour in the chambers, which minimises frost condensation on the ice surface during the experiments.

[2] Circulating dry nitrogen discharges air that contains water vapour in the tubes in the Cryo-SEM preparation system. If a large amount of water vapour remains in the tubes, condensed vapour produced by the cooled gas could clog the tubes (Fig. 1).

step size, which varied from 0.02–0.5 μm. The accelerating voltage was 30 kV and the beam current was 9.2 nA (for a spot size of 6.0) in this assessment. Step sizes of 0.2 μm or above produced the clearest Kikuchi patterns. Below 0.2 μm, recognizable patterns were absent because of radiation damage. Compared with ESEM, radiation damage is considerably higher in a high-vacuum SEM, which results in typical damage widths of 0.5 μm (Fig. 6 in Weikusat *et al.*, 2011a). We analysed a series of Kikuchi patterns obtained with a step size of 0.2 μm to evaluate the spatial resolution of our system. The line scan analysis in the direction parallel to the sample tilt axis (x-direction) yielded three Kikuchi patterns with bands originating from neighbouring grains. The spatial resolution in this direction is therefore 0.2 μm×3=0.6 μm. The spatial resolution in the direction perpendicular to the sample tilt axis (y-direction) is 1.8 μm, which is three times that in the x-direction because of the tilt angle of 70° (Humphreys, 2001). The spatial resolution in the tilt direction is close to the value of 0.5 μm reported by
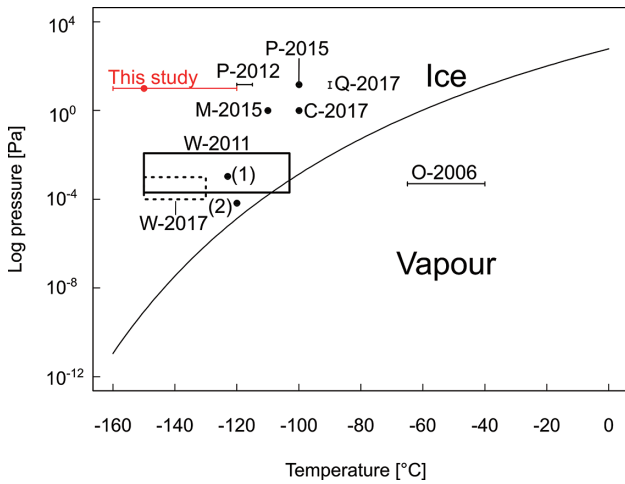
Fig. 10. Phase diagram of ice showing the temperature–logarithm-of-pressure space explored in this study to optimise electron backscattered diffraction mapping. Boundary between Ice and Vapour is drawn following Bielska *et al.* (2013). Red line and dot represent temperature and pressure used in this study, while black lines, dots and squares represent those used in previous studies (O-2006: Obbard *et al.* (2006), W-2011: Weikusat *et al.* (2011a), P-2012: Prior *et al.* (2012), P-2015: Prior *et al.* (2015), M-2015: Montagnat *et al.* (2015), W-2017: Weikusat *et al.* (2017b), C-2017: Chauve *et al.* (2017), Q-2017: Qi *et al.* (2017)). (1) and (2) indicate data from W-2011 used for spatial resolution analyses (see Appendix 3).

Weikusat *et al.* (2011a) who used a different experimental setup (1.1×10^{-3} Pa, -123°C, defocussed beam; and 6.7×10^{-3} Pa, -120°C, with slight sublimation of the ice sample; Fig. 10).

Appendix 4. Assessment of errors in misorientation angle between neighbouring pixels

To estimate the error of misorientation angles between neighbouring pixels, we focussed on misorientation angles with values between 0.1° and 4° obtained from strain-free annealed artificial ice samples. We calculated averages of these misorientation angles (hereafter [MO]$_{mean}$) from maps obtained with different step sizes. The error was defined as [MO]$_{mean} + 2\sigma$, where σ denotes the standard deviation. For all step sizes, [MO]$_{mean} + 2\sigma$ was 0.6°–0.8°. Most misorientation angles (97%) were within the range [MO]$_{mean} \pm 2\sigma$ for all step sizes. The error of our EBSD analysis is similar to that reported for other studies of ice and metals (0.5°–1°; Humphreys *et al.*, 1999; Krieger Lassen, 1996; Weikusat *et al.*, 2011a). By averaging the map data (Humphreys *et al.*, 2001) using the Advanced Kuwahara filter with a window size of 5×5 pixels in Tango, the error is reduced to 0.4° ([MO]$_{mean} + 2\sigma = 0.2° + 2 \times 0.1° = 0.4°$).